Proceedings of the 33rd International Conference on Ocean, Offshore and Arctic Engineering
OMAE2014
June 8-13, 2014, San Francisco, California, USA

OMAE2014-24427

TURBULENCE MODELING, LOCAL GRID REFINEMENT AND ABSORBING BOUNDARY CONDITIONS FOR FREE-SURFACE FLOW SIMULATIONS IN OFFSHORE APPLICATIONS

Arthur E.P. Veldman*
Roel Luppes
Henri J.L. van der Heiden
Peter van der Plas
Institute for Mathematics and Computer Science
University of Groningen
P.O. Box 407, 9700 AK Groningen
The Netherlands
{a.e.p.veldman, r.luppes, h.j.l.van.der.heiden, p.van.der.plas}@rug.nl

Bülent Düz
René H.M. Huijsmans
Department of Ship Hydrodynamics
Technical University of Delft
Mekelweg 2, 2628 CD Delft
The Netherlands
{r.h.m.huijsmans, b.duz}@tudelft.nl

ABSTRACT

To study extreme hydrodynamic wave impact in offshore and coastal engineering, the VOF-based CFD simulation tool ComFLOW is being developed. Recently, much attention has been paid to turbulence modeling, local grid refinement, wave propagation and absorbing boundary conditions. The turbulence model has to cope with coarse grids as used in industrial applications. Thereto a blend of a QR-model and a regularization model has been designed, in combination with a dedicated wall model. Local grid refinement is based on a semi-structured approach. Near refinement interfaces special discretization stencils have been designed. The computational domain is restricted to the close environment of the objects studied. To suppress unphysical reflections, special generating and absorbing boundary conditions have been designed. The combined performance of the new ingredients will be demonstrated with several applications. For validation, experiments have been carried out at MARIN.

INTRODUCTION

Extreme hydrodynamic wave impact on rigid and floating structures is of high industrial interest in offshore and coastal engineering. To study the occurring phenomena the CFD VOF-based simulation tool ComFLOW has been developed; see e.g. [1, 2]. Over the years, several physical modeling aspects and numerical algorithmic issues have been tackled. In the early phase of the ComFLOW development, emphasis has been on simulating momentum-dominated phenomena, such as the impact of extreme waves (e.g. green water loading [3] and wave run-up) and on sloshing (e.g. in LNG tanks [4]). In these applications viscous effects can be mostly neglected. Furthermore, the oncoming and outgoing waves were assumed to be two-dimensional (including the reflected and radiated waves), which gave a restrictive limitation to the usefulness of the method.

Later, the application area has been extended to flows where the influence of viscosity is becoming noticeable, like in side-by-side mooring or inside moonpools. Thus, recently much attention has been paid to turbulence modelling. One has to realize that the grids used in ComFLOW will be too coarse to resolve the turbulent details of the flow. Therefore a turbulence model is required that can cope with coarse grids, yet without excessive diffusive smoothing. Based on recent developments in turbulence modeling, a blend of a QR-model and a regularization model has been designed along the lines of [5]. Near solid walls a dedicated wall model (Werner-Wengle [6]) is applied. Numerical oscillations caused by the coarse grid are reduced by applying

*Address all correspondence to this author.

(classical) limiting [7].

Also the character of the oncoming and reflected waves has been extended to become fully three dimensional in arbitrary orientation w.r.t. the computational boundary (i.e. multi-directional). Thus a rather general type of generating and absorbing boundary conditions (GABC) has been developed, inspired by the higher-order Sommerfeld-type of boundary conditions introduced by Higdon [8]. A special feature is the use of an approximate dispersion relation [9] to provide the estimate for the propagation speed required by Sommerfeld-type conditions. With these GABCs, the computational effort can be decreased significantly by restricting the computational domain to the close environment of the objects studied.

Grid resolution can be enhanced by using local grid refinement. Hereto, a semi-structured approach [10] is used on rectangular refinement regions allowing efficient solution methods. Near refinement interfaces special discretization stencils have been designed, as well as an adaptation of the VOF algorithm to move the free liquid surface.

The performance of the new ingredients will be demonstrated with several applications, such as a dambreak (where viscosity plays no role), a semi-submersible in waves, and sloshing in a moonpool (with non-negligible viscous influence). For both applications, experiments have been carried out at MARIN to validate the computational results.

BASIC MODELLING

The incompressible, turbulent fluid flow is modelled by means of the Navier–Stokes equations.

$$\mathscr{M}u = 0, \qquad \frac{\partial u}{\partial t} + \mathscr{C}(u)u + \mathscr{G}p - \mathscr{D}u = f. \tag{1}$$

Here $\mathscr{M}$ is the divergence operator[1] which describes conservation of mass. Conservation of momentum is based on the convection operator $\mathscr{C}(u)v = \nabla(u \otimes v)$, the pressure gradient operator $\mathscr{G} = \nabla$, the diffusion operator $\mathscr{D}(u) = \nabla \cdot \nu \nabla u$ and forcing term f. The kinematic viscosity is denoted by ν.

The second-order finite-volume discretization of the continuity equation at the new time level $\cdot^{(n+1)}$ is given by

$$M^0 u_h^{(n+1)} = -M^\Gamma u_h^{(n+1)}, \tag{2}$$

where M^0 acts on the interior of the domain and M^Γ acts on the boundaries of the domain. In the discretized momentum equation, convection $C(u_h)$ and diffusion D are discretized explicitly in time. The pressure gradient is discretized at the new time level. In this exposition, for simplicity reasons the first-order forward Euler time integration will be used. In the actual calculations, the second-order Adams–Bashforth method is being applied.

Taking the diagonal matrix Ω to denote the matrix containing the volumes of the control volumes, gives the discretized momentum equation as

$$\Omega \frac{u_h^{(n+1)} - u_h^{(n)}}{\delta t} = -C(u_h^{(n)})u_h^{(n)} + Du_h^{(n)} - Gp_h^{(n+1)} + f. \tag{3}$$

The discrete convection operator is skew-symmetric, i.e.

$$C(u_h^{(n)}) + C(u_h^{(n)})^T = 0, \tag{4}$$

where the superscript $\cdot^T$ denotes the transpose. In this way convection does not contribute to energy production or dissimination [11]; in particular its discretization does not produce artificial viscosity. To make the discretization fully symmetry-preserving, the discrete gradient operator and the divergence operator are each others negative transpose, i.e. $G = -M^{0T}$, thus mimicking analytic symmetry $(\nabla\cdot) = (\nabla)^T$, as in [11]. The solution of this equation is split into two steps. An auxiliary variable $\tilde{u}_h$ is defined through the equation

$$\Omega \frac{\tilde{u}_h - u_h^{(n)}}{\delta t} = -C(u_h^{(n)})u_h^{(n)} + Du_h^{(n)} + f. \tag{5}$$

Imposing discrete mass conservation (2) on the new time level $(n+1)$ results in a linear system for the pressure:

$$\delta t\, M^0 \Omega^{-1} G\, p^{(n+1)} = M^0 \tilde{u}_h + M^\Gamma u_h^{(n+1)}. \tag{6}$$

This equation is often referred to as the discrete pressure Poisson equation, as it can be regarded to be a discretization of the equation $\mathscr{M}\mathscr{G}p_h = \mathscr{M}\tilde{u}$.

DISCRETIZATION AND LOCAL GRID REFINEMENT

The Navier–Stokes equations (1) are discretized on an Arakawa C-grid as illustrated in Fig. 1. For brevity the third dimension, which is treated similarly, is omitted. The subscript ℓ is used to indicate the local refinement level, where $\ell = 0$ refers to the unrefined base grid (indexing is discussed below). In the regular parts of the grid the divergence operator is discretized as follows (for the subscript convention consult Fig. 1)

$$Mu_h|_\ell = \delta y_\ell (U_{e;\ell} - U_{w;\ell}) + \delta x (V_{n;\ell} V_{s;\ell}).$$

[1] Note that calligraphic symbols denote analytic operators, whereas their discrete counterparts will be denoted by upper-case symbols.

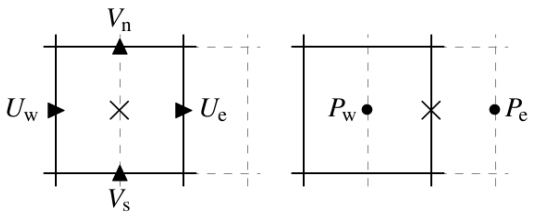

FIGURE 1. REGULAR DISCRETIZATION STENCIL FOR Mu_h (LEFT) AND THE x-COMPONENT OF Gp_h (RIGHT) APPLIED AT THE LOCATION INDICATED WITH $\times$.

In order to let the discrete operators satisfy the adjoint condition, $G = -M^T$, the pressure gradient is discretized as $Gp_h = -M^{0T} p_h$. This gives the following second-order central discretization:

$$\frac{P_{e;\ell} - P_{w;\ell}}{\delta x} \quad \text{and} \quad \frac{P_{n;\ell} - P_{s;\ell}}{\delta y}.$$

Refinement approach

A semi-structured approach [10] is followed in which a cell (i, j) at refinement level ℓ is replaced by a set of $r_i \times r_j$ smaller cells at refinement level $\ell+1$ having indices $(2i+m, 2j+n)$ at offsets $0 \le m < r_i,\ 0 \le n < r_j$. The semi-structured indexing system is illustrated in Fig. 2. On block-shaped refinement regions the method is locally structured, hence the computational efficiency of the original array-based solution methods can be exploited as much as possible. Only at the boundaries of the refinement regions where the actual refinement takes place a new treatment is required. For describing the grid lay-out an auxiliary array is introduced storing only one integer for each potentially occurring cell $(i, j; \ell)$ pointing at the memory location of the subgrid in which it is contained (or null if the cell does not exist). Thus, along the lines of [10] a data structure results that allows for fast and efficient look-up when compared with typical tree-based storage methods.

In the results presented below, the refinement regions have been kept constant throughout the simulation and chosen with physical insight: where are many flow details in action? Under development is an adaptive refinement strategy that is controlled by the local vorticity in the flow.

Poisson equation near interfaces

Near refinement interfaces the discretization stencil is incomplete due to 'missing' coarse or fine grid variables. Typically, a large stencil is used for the approximation of missing pressure or velocity variables along the refinement interface. Interpolation of missing variables increases the number of non-zero

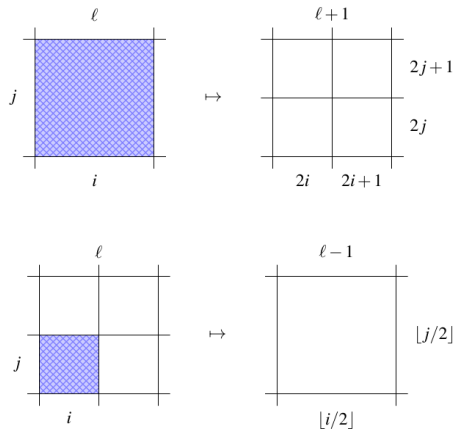

FIGURE 2. ILLUSTRATION OF SEMI-STRUCTURED INDEXING FOR REFINEMENT RATIOS $r_i = 2$, $r_j = 2$. TOP: FROM COARSE TO FINE INDICES. BOTTOM: FROM FINE TO COARSE INDICES.

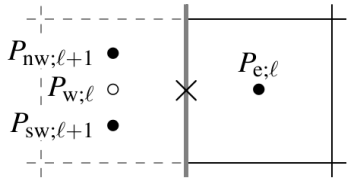

FIGURE 3. REFINEMENT WITH SHIFTED PRESSURE GRADIENT WHICH IS EQUAL FOR BOTH REFINED CELL FACES. MISSING VARIABLES ARE DENOTED BY .

coefficients in the pressure Poisson matrix, which might result in a non-symmetric matrix, putting higher demands on the solver. Most authors use a non-overlapping interface and apply linear (or even higher-order) interpolation for missing variables on the other side of the interface [12]. Another approach is to apply linear interpolation inside an overlapping interface [13]. In all of these cases the discretization results in a non-symmetric system of equations.

In the present approach, a compact discretization scheme is designed (in particular for the implicit part) that results in a small and symmetric scheme for the discrete composition of M and G. E.g. the discrete gradient at the interface is computed according to Fig. 3; compare [14, 15]. This makes it possible to employ an efficient linear solver. Furthermore, it facilitates the use of adjacent refinement regions as well as the interface discretization near objects and free-surface boundaries.

Dambreak experiment

To demonstrate the validity of the local refinement method for practical cases, it is tested for the simulation of a breaking

dam. ComFLOW has been used before for this classical test [1], therefore it provides good material for assessing the performance of the local refinement method. Note that no turbulence model is applied, as viscosity plays only an insignificant role in this application.

As starting point for the refinement (or better: for the coarsening), a grid is used of $200 \times 36 \times 50$ points. In order to save computational time, the original resolution is only maintained around the block; to the right as well as towards the sides of the domain it is coarsened (as illustrated in Fig. 4).

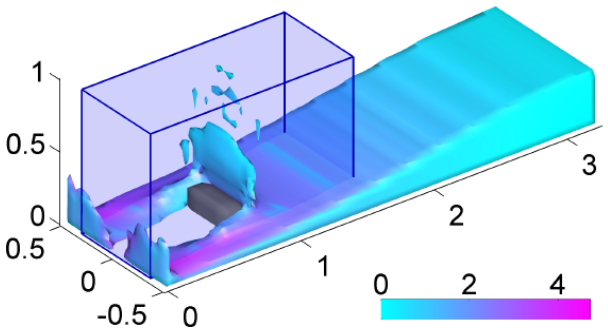

FIGURE 4. GEOMETRY OF THE DAMBREAK SIMULATION INDICATING THE REFINEMENT REGION: THE ORIGINAL RESOLUTION IS ONLY KEPT INSIDE THE DASHED BOX. THE ISOSURFACE OF THE VOLUME FRACTION IS COLORED BY THE ABSOLUTE VELOCITY AT THE FREE SURFACE.

The simulation results in Fig. 5 show good correspondence with the measurements and it can be seen that coarsening in the region of the reservoir does not affect the prediction of the impact pressure. The differences between the locally coarsened grid versus the uniformly-fine grid are much smaller than the actual modelling error while the computational time has been reduced from 8h05' to 0h38'. This illustrates that for typical impact problems a significant computational saving can be made by coarsening in the far-away regions.

SURFACE RECONSTRUCTION AND ADVECTION

Spurious energy dissipation in numerical wave simulations can be due to the discretization method used for the governing equations applied inside the flow domain, but can also be due to the numerical implementation of the moving free surface and the boundary conditions applied at the free surface. Here, we investigate the effect of various VOF-methods: in particular we investigate Simple Line Interface Calculation (SLIC) [16] and Piecewise Linear Interface Calculation (PLIC) [17]. In the VOF-approach a scalar indicator function f (with $0 \leq f \leq 1$) characterizing the volume fraction f occupied by one of the fluids

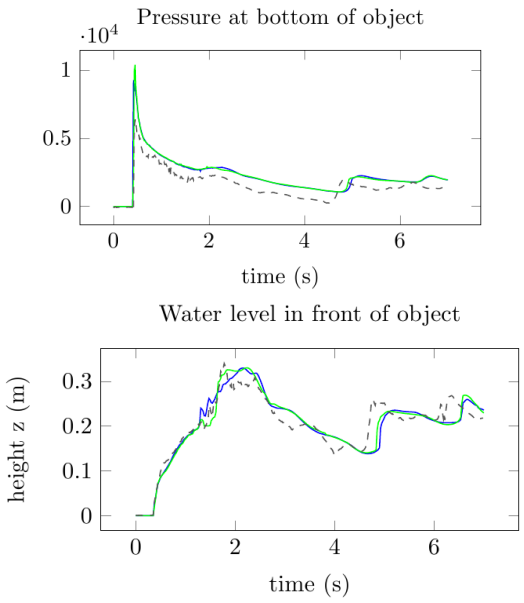

FIGURE 5. NUMERICAL RESULTS AND MEASUREMENTS FOR THE 3-D DAMBREAK EXPERIMENT. LEGEND: 'blue' COARSENED GRID; 'green' UNIFORM GRID; 'dashed' EXPERIMENT.

within each cell, is advected (for solenoidal flow) by the following transport equation

$$\frac{\partial f}{\partial t} + \nabla \cdot (uf) = 0. \tag{7}$$

To preserve the steep profile of the interface, the explicit location of the interface is locally reconstructed and corresponding volume fluxes are computed to update the volume fraction field to the next discrete time level using Eq. (7). For a review of interface reconstruction methods, see, e.g., [18, 19]. Once the interface is reconstructed, the volume fraction field is conservatively advected in time via Eq. (7). This equation can be solved using either an unsplit advection or a direction split advection scheme. The latter are more common in standard VOF-methods due to ease of implementation.

Here, we compare a few interface reconstruction/advection combinations in simulations of propagating waves. For advection, we will use the COSMIC (Conservative Operator Splitting for Multidimensions with Inherent Constancy) scheme of Leonard et al. [20] which in a 2D (x,z)-plane[2] can be written as

$$f^X \equiv f^{(n)} - \delta t \frac{\partial u f^{(n)}}{\partial x} + \delta t f^{(n)} \frac{\partial u}{\partial x}$$

[2]Throughout the paper, a right-handed coordinate system is used, with the x-axis in longitudinal flow direction, whereas the z-axis points in vertical direction.

$$f^Z \equiv f^{(n)} - \delta t \frac{\partial w f^{(n)}}{\partial z} + \delta t f^{(n)} \frac{\partial w}{\partial z} \tag{8}$$
$$f^{(n+1)} \equiv f^{(n)} - \delta t \left[\frac{\partial}{\partial x} \left(u \frac{f^{(n)} + f^Z}{2} \right) + \frac{\partial}{\partial z} \left(w \frac{f^{(n)} + f^X}{2} \right) \right].$$

We compare it with the current VOF implementation in the CFD simulation tool ComFLOW. It employs the SLIC-VOF method introduced by Hirt and Nichols [16] combined with a local height function (LHF) [21] to overcome the bottlenecks which originate from this VOF-technique such as violation of mass conservation and spurious flotsam and jetsam.

In a PLIC-VOF method, the interface in each cell is approximated by a line (or a plane in three dimensions). Within each cell, the approximated interface can be defined by the equation: $n \cdot x = \alpha$, where n is the local surface normal, x is the position vector of a point on the interface and α is a constant. Among many techniques that are available in the literature for computing n, we will show results for three methods: Youngs algorithm [17], the least-square gradient (LSG) technique by Rider and Kothe [18] and the Mixed Youngs Centered (MYC) implementation of Aulisa et al. [22]. Hereafter, α can be calculated analytically [23].

Reversible deformation

In the test problem, a sphere of radius 0.15 and center (0.35, 0.35, 0.35) is immersed in a 3D reversible deformation field inside a unit sized cube. The flow is formed by the velocity field:

$$u = 2\sin^2(\pi x)\sin(2\pi y)\sin(2\pi z)\cos(\pi t/T),$$
$$v = -\sin(2\pi x)\sin^2(\pi y)\sin(2\pi z)\cos(\pi t/T),$$
$$w = -\sin(2\pi x)\sin(2\pi y)\sin^2(\pi z)\cos(\pi t/T),$$

where $T = 3$ is used. Due to this velocity field, the sphere undergoes severe deformation until it reaches maximum stretching at $t = 1.5$, then returns to its initial shape.

Fig. 6 shows the results on a $128 \times 128 \times 128$ grid using the H&N + LHF method versus the LSG + COSMIC combination at time t = 1.5 and t = 3. The LSG + COSMIC scheme clearly outperforms the H&N + LHF method. This is also reflected in Tab. 1 which shows, for a series of grids, the geometrical error $E = ||f(t=3) - f(t=0)||_1$, i.e. the L_1-norm of the f-difference between $t = 3$ and $t = 0$.

Propagating Rienecker-Fenton waves

A further example are propagating Rienecker-Fenton waves in shallow water. Here, we particularly focus our attention on investigating the effect of various interface-reconstruction/advection combinations on energy dissipation.

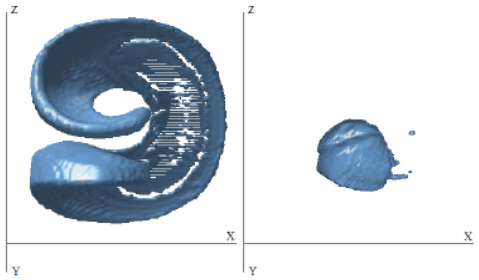

(a) H&N + LHF

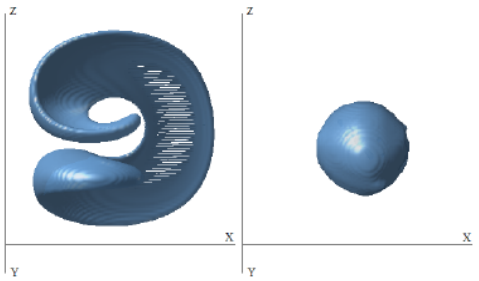

(b) LSG + COSMIC

FIGURE 6. 3D REVERSIBLE DEFORMATION FIELD TEST ON A 128^3 GRID AT $CFL = 0.5$. SNAPSHOTS ARE TAKEN AT MAXIMUM DEFORMATION ($t = 1.5$), AND AFTER THE FLOW RETURNS BACK ($t = 3$). TOP: H&N + LHF; BOTTOM: LSG + COSMIC.

Mesh	Youngs+COSMIC	LSG+COSMIC	H&N+LHF
32^3	7.66×10^{-3}	7.51×10^{-3}	1.06×10^{-2}
	(1.56)	(1.68)	(1.05)
64^3	2.59×10^{-3}	2.34×10^{-3}	5.1×10^{-3}
	(1.78)	(1.81)	(1.08)
128^3	7.50×10^{-4}	6.64×10^{-4}	2.4×10^{-3}

TABLE 1. L_1-ERRORS FOR THE 3D DEFORMATION FIELD AT $CFL = 0.5$. THE ORDER OF ACCURACY OF A METHOD IS BETWEEN PARENTHESES.

We consider a wave of period $T = 4sec$, wave height $H = 2m$, wave length $L = 26.1m$ and steepness 7.6%. The water depth $D = 9.5m$. The incoming wave is started from rest (wave amplitude zero); the incoming wave height then is growing gradually over time until it reaches its final value (this is to avoid a too violent initial reaction on the incoming wave).

To exaggerate the difference between the various reconstruction/advection combinations, a coarse grid, with mesh size $\delta x = \delta z = 1m$ has been used. Figure 7 shows the surface elevation as a function of the position after $t = 200sec$. The re-

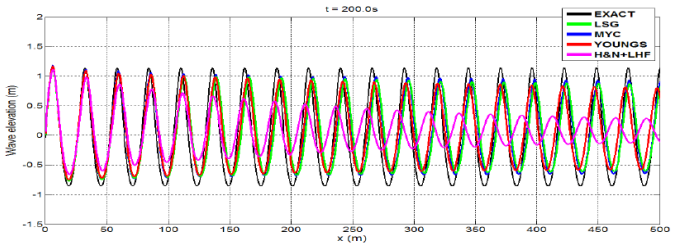

FIGURE 7. WAVE ELEVATION AS A FUNCTION OF HORIZONTAL LOCATION FOR A WAVE WITH STEEPNESS 7.6%. THE LSG, MYC AND YOUNGS METHODS ARE COMBINED WITH THE COSMIC ADVECTION SCHEME. THE GRID RESOLUTION HAS BEEN TAKEN VERY COARSE TO EXAGGERATE THE DIFFERENCES.

sults are obtained using several PLIC algorithms with the COSMIC advection scheme. Also, the analytical results from the Rienecker-Fenton theory and the Hirt-Nichols VOF with local height function (H&N + LHF) are plotted in the figure. The results on this coarse grid in Fig. 7 demonstrate that the behavior of Hirt-Nichols VOF + LHF is considerably dissipative: the wave lost nearly 78% of the initial wave height after 17 consecutive wave lengths. Additionally, this method causes a clear phase shift with respect to the analytical solution. When the PLIC algorithms + COSMIC advection combinations are used, results improve substantially as less dissipation and phase shift are observed: 70% of the initial wave height remains with Youngs' method after 17 wave lengths, whereas 75% remains with the LSG and MYC methods. In terms of phase shift, there is only a slight difference between the reconstruction methods.

ABSORBING BOUNDARY CONDITIONS

For efficient computational modeling, the vast spatial domain around the region of interest is truncated via artificial boundaries, which may induce unphysical reflections of a numerical solution. Thus, developing robust and efficient boundary conditions to be imposed on these artificial boundaries is an important numerical goal. Usually, these are called non-reflecting or absorbing boundary conditions (ABCs) [24].

Dispersive ABC

The Sommerfeld radiation condition is the cornerstone of non-reflecting boundary conditions. It can be generalized on the x-outflow boundary as

$$\left(\cos\alpha\,\frac{\partial}{\partial t}+c\,\frac{\partial}{\partial x}\right)\phi=0. \tag{9}$$

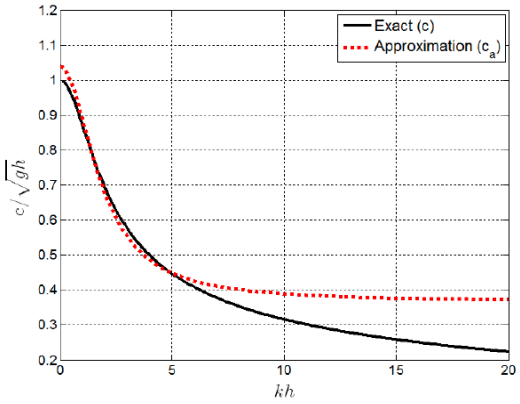

FIGURE 8. APPROXIMATION OF THE DISPERSION RELATION. FOR THE COEFFICIENTS IN EQ. (11), $a_0 = 1.04$, $a_1 = 0.106$ AND $b_1 = 0.289$ ARE USED.

Higdon [8] showed that Eq. (9) is perfectly absorbing if α is equal to the angle of incidence θ for a wave described by the wave or velocity potential ϕ and travelling with phase speed c. If we replace c in Eq. (9) by the familiar dispersion relation, we can rewrite it as

$$\left(\cos\alpha\,\frac{\partial}{\partial t}+\sqrt{gh}\sqrt{\frac{\tanh(kh)}{kh}}\,\frac{\partial}{\partial x}\right)\phi=0, \tag{10}$$

where g denotes the gravitational acceleration, whereas h is the water depth. The boundary condition (10) is perfectly absorbing for this single component. Recall that any solution can be represented by a linear superposition of waves, where each individual component of this irregular wave has its own frequency, amplitude, wave number and phase. Therefore, the boundary condition (10) cannot annihilate all these wave components simply because it is evidently designed for only one of them.

At this point a question crosses one's mind: Is it possible to develop a boundary condition which has the feature of allowing reflection only to an acceptable threshold for all the wave components which all together form an irregular wave? One can deduce from the way this question is asked that we expect some amount of reflection for such a boundary condition but it will be restricted within certain limits.

Hereto, we introduce the following rational expression which approximates the dispersion relation:

$$c_a \approx \sqrt{gh}\,\frac{a_0+a_1(kh)^2}{1+b_1(kh)^2}, \tag{11}$$

where a proper choice of coefficients a_0, a_1 and b_1 would lead to a close approximation for the largest possible range of kh-values,

see Fig. 8. Thus, reflection from the boundary will be minimized over that specific range of kh-values. As a result of strong effects of dispersion, especially in deep water, any wave behaves as the sum of a large number of wave components, each travelling at its own dispersive phase speed. To compute these local velocities we will exploit the exponential behavior of the wave potential in the z-direction. Thus, assuming the wave potential to be of the form $\phi(x,y,z) = \psi(x,y)e^{\pm kz}$ (note that the wave number k may be imaginary to represent evanescent waves), it follows that

$$\frac{\partial^2\phi}{\partial z^2} = k^2\phi. \tag{12}$$

Now we substitute Eqs. (11) and (12) into Eq. (10) to reach the final form of the absorbing boundary condition (ABC) in x-direction:

$$\left(1+b_1h^2\frac{\partial^2}{\partial z^2}\right)\cos\alpha\,\frac{\partial\phi}{\partial t}+\sqrt{gh}\left(a_0+a_1h^2\frac{\partial^2}{\partial z^2}\right)\frac{\partial\phi}{\partial x}=0. \tag{13}$$

In our wave applications, the potential ϕ is related to the flow variables at the boundary by

$$\frac{\partial\phi}{\partial x}=u, \quad \text{and} \quad \frac{\partial\phi}{\partial t}=-\frac{p}{\rho}-gz.$$

Substituting this in the ABC results in a boundary condition featuring u, p and their second-order derivatives in z-direction. Its discretization generates a larger stencil than usual, but imposes no special complications.

Wave reflection

In case of a mismatch between the numerical and physical wave direction (α versus θ), and/or numerical and physical wave speed (c or c_a versus c^{out}), the wave will partly reflect against the outflow boundary. Its reflection coefficient is given by

$$R_{Higdon} = -\frac{c^{out}\cos\alpha - c\cos\theta}{c^{out}\cos\alpha + c\cos\theta}. \tag{14}$$

For the numerical approximation this changes into

$$R_{ABC} = -\frac{(1+b_1(kh)^2)c^{out}\cos\alpha - \sqrt{gh}(a_0+a_1(kh)^2)\cos\theta}{(1+b_1(kh)^2)c^{out}\cos\alpha + \sqrt{gh}(a_0+a_1(kh)^2)\cos\theta}. \tag{15}$$

Figure 9 demonstrates the amount of reflection as a function of the angle of incidence θ and dimensionless wave number kh to compare the effectiveness of the two boundary conditions: the

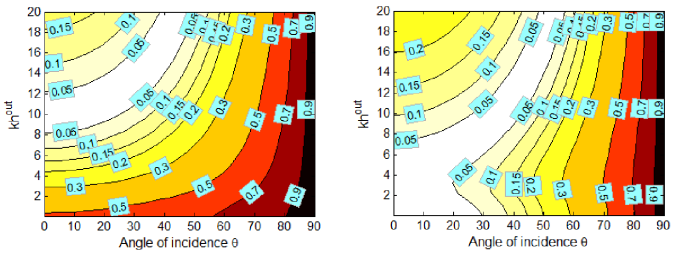

FIGURE 9. AMOUNT OF REFLECTION (IN PERCENT) AS A FUNCTION OF THE ANGLE OF INCIDENCE θ AND kh WHEN VARIOUS BOUNDARY CONDITIONS ARE USED: (LEFT) HIGDON EQ. (9); (RIGHT) ABC EQ. (13). $\alpha = 0$ AND $c = 0.316\,gh$ IS TAKEN IN BOTH BOUNDARY CONDITIONS. REFLECTION VALUES ARE PLOTTED ON THE CONTOUR LINES.

Higdon operator (9) and the first-order ABC (13). For the coefficients in Eq. (13) we take $a_0 = 1.04$, $a_1 = 0.106$ and $b_1 = 0.289$. We also take $c = 0.316\,gh$ in the boundary conditions in which this parameter appears. This choice corresponds to the kh-value of 10 which is exactly in the middle of the considered kh-range between 0 and 20. All the angle parameters in the boundary conditions are set to be zero as an arbitrary initial choice. In Fig. 9, light-colored areas between isolines illustrate small reflection zones while as the color gets darker the amount of reflection increases since grazing incidence is approached where waves propagate parallel to the outflow boundary. More particularly, white-colored zones demonstrate the ranges where the reflection coefficient is below 5% which is an acceptable threshold in practical wave simulations. Close examination of the results clearly shows the relative merits of ABC over the first-order Higdon operator.

The first-order Higdon operator Eq. (9) generates reflection below 5% between kh-values of 8 to 12 approximately, which is expected since the prespecified c-value corresponds to the kh-value of 10. However, this range is between 0 to 8 with the ABC in Eq. (13). The reason for this behavior lies in the way the dispersion relation is approximated. The area between the two lines in Fig. 8 gives an indication of the amount of reflection caused by the approximation. From this plot, we clearly see that the dispersion relation is approximated well in the range $kh \in [0,8]$. From 8 to 20, the reflection increases as the approximation becomes gradually poor, which is shown in Fig. 9(right). In terms of directional effects, the performance of the ABC is somewhat better than the first-order Higdon operator.

Semi-submersible in waves

As a first 'practical' demonstration of the GABC boundary condition, Fig. 10(top) shows the geometry of a semi-submersible that has been tested in the MARIN basin; also the position of some measurement probes has been indicated. The

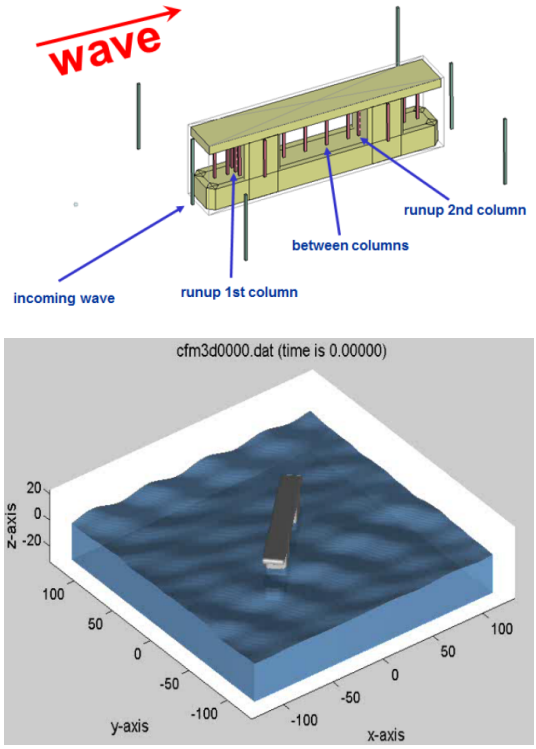

FIGURE 10. TOP: GEOMETRY OF THE SEMI-SUBMERSIBLE TESTED IN INCOMING WAVES. BOTTOM: THE COMPUTATIONAL DOMAIN AND THE WAVE PATTERN FROM A SIMULATION USING GABC.

bottom part of Fig. 10 shows the computed wave pattern around the semi-submersible; the full computational domain is shown. Special attention should be paid to the behaviour of the free surface near the domain boundaries: no visible reflections can be detected. We will report on detailed comparisons between simulations and experiments in forthcoming publications.

TURBULENCE MODELLING

In order to simulate the high Reynolds number turbulent flows that are associated to offshore applications, some form of turbulence modeling is required. Simply put, it is necessary to model those scales of motion that cannot be represented on the computational grid, i.e. the subgrid scales. The production of small scales takes place through the non-linear convective term. The only mechanism that counteracts the production of small scales of motion is diffusion. The equilibrium between production (by convection) and dissipation (by diffusion) of small scales cannot be reached on the computational grid. This consideration gives rise to two modeling options: either restrict the production of subgrid scales or increase the dissipation of subgrid scales.

Important information of the physics of turbulent flows is contained in the invariants of the rate-of-strain tensor

$$S(u) = \nabla u + (\nabla u)^T.$$

As is shown in [25], the rate of dissipation of the scales contained in a domain Ω_Δ of size Δ, can be expressed in terms of the second invariant $q(u)$ of $S(u)$ as

$$Q(u) \equiv \int_{\Omega_\Delta} q(u)\,\mathrm{d}\Omega \equiv \int_{\Omega_\Delta} \tfrac{1}{2}\mathrm{tr}\, S^2(u)\,\mathrm{d}\Omega. \tag{16}$$

The third invariant, denoted by $r(u)$ can be integrated over the same domain to give

$$R(u) \equiv \int_{\Omega_\Delta} r(u)\,\mathrm{d}\Omega \equiv \int_{\Omega_\Delta} \tfrac{1}{3}\mathrm{tr}\, S^3(u)\,\mathrm{d}\Omega = \int_{\Omega_\Delta} \det S(u)\,\mathrm{d}\Omega. \tag{17}$$

When positive, the quantity (17) gives a measure for the convective production of scales smaller than Δ. If negative, energy is transferred from subgrid-scale structures to the resolved scales. In order to separate the scales properly, a turbulence model should close the transfer of energy in either direction.

QR eddy-viscosity model

The analysis in [25] shows that in order to arrive at an appropriate eddy-viscosity model, we evaluate the eddy-viscosity in terms of the invariants as

$$\nu_{\mathrm{eddy}} = \frac{3}{2}\frac{|R(u)|}{\lambda_\Delta Q(u)} \tag{18}$$

where λ_Δ is the eigenvalue of the discrete diffusive operator corresponding to the scale Δ. Taking Δ identical to the grid size, this eigenvalue is a measure for the dissipation of the smallest resolvable scales. We will refer to this model as the QR-model.

Note that the classical Smagorinsky turbulence model (see e.g. [26]) is formulated in terms of the invariant Q only, and dissipates energy also on well-resolved (even laminar) scales in the flow.

Regularization modeling

In order not to interfere with the subtle energetic balance between the convection and diffusion in a turbulent flow on resolved scales, it is important to preserve the symmetries of the Navier–Stokes equations on a discrete level [11]. A symmetry-preserving regularization of the convective term smooths the original convective term while preserving its skew-symmetry. The smoothing takes place through a filter operation $u_h \to \overline{u_h}$.

Verstappen [27] applies the filter to the convective term, which yields a family of symmetry-preserving regularization models. For the discrete convective term $C(u_h)u_h$, the second-order (in terms of the filter length) accurate regularization model from this family is given by

$$C_2(u_h,u_h) = \overline{C(\overline{u_h})\,\overline{u_h}}. \tag{19}$$

Selfadjointness of the filter ensures the skew-symmetry of the original convective term. The length scale over which the filter smoothes the signal will depend on the local flow physics. The analysis in [28] shows that an expression for damping of the convective production of structures beyond length scale Δ can be derived. The damping factor, denoted by f_2, is a functional of the (local) filter length α, i.e. $f_2 = f_2(\alpha(u))$. Balancing the convective production of subgrid scales and the natural diffusive dissipation gives

$$f_2(\alpha)\frac{|R(u)|}{Q(u)} = \nu|\lambda_\Omega|, \tag{20}$$

from which the filter length can be determined. The relation with (18) is evident.

A blended model

In practice we use a blended model, in which both the QR eddy-viscosity model and the regularization model play a role [5]. The transfer of energy from resolved to subgrid scales (i.e. (17) is positive) is modeled by the QR eddy-viscosity model. The backscatter of energy from subgrid scales to resolved scales (i.e. (17) is negative) is prevented by the regularization model. The mixture of these models allows for a complete separation of resolved and subgrid scales. Only if the energy is transferred to smaller scales of motion, the kinetic energy is dissipated from the resolved flow structures. The model is closed for backscatter by the regularization of the nonlinear convective interaction between subgrid and resolved scales. If, because of the quite coarse grids, some oscillations remain in the numerical solution, these are smoothened by means of a 'minmod' limiter [7].

This type of turbulence modeling, which tries to add only minimal turbulent diffusion (= eddy viscosity), is quite recent and has been validated thus far on turbulent channel flow [27] and on differentially-heated cavities [29]. Currently it is being tested for more industrial applications in aerospace and maritime engineering, with very promising results (Verstappen, private communication, 2014). It is hoped that this type of model can also deal with the turbulence near a free surface, which is two-dimensional in character and for which 'traditional' turbulence models do not apply. We plan to test this in the near future.

The near-wall boundary layer

From a computational point of view it is undesirable to refine the grid to the level at which the boundary layer can be resolved. In order to account for the influence of the turbulent boundary layer on the effective wall-shear stress that the outer flow experiences, the Werner–Wengle model is applied [6].

Moonpool water motion

The simulation of free-surface dynamics in moonpools is an example of an application where possibly violent free-surface motion is coupled to viscous flow details. A realistic simulation of free-surface motion is strongly dependent on the correct prediction of the vortex formation in the moonpool. The combination of coarse grids and upwind discretization techniques dissipates the perturbations that lead to the characteristic roll-up of the shear layer, thus preventing vortex formation at the edges of the moonpool. In order to illustrate the performance of the above-described central discretization, the first results of the simulation of water motion in a moonpool (in calm water) will be presented.

In order to model moonpool dynamics in calm water (i.e. in the absence of waves) not the entire ship will be modeled. The domain has dimensions (in m) $[5.0,6.0]\times[0.5,0.5]\times[4.0,0.5]$, and the stretched grid has dimensions $228\times10\times184$. As the setup of the problem is two-dimensional and most variation is expected to take place in the (x,z)-plane, we assume that 10 uniformly spaced grid points in the are y-direction are enough to capture the essential physics. The smallest grid spacing is $0.01m$.

In rest, the flat free-surface $(z=0)$ is elevated $0.4m$ above the submerged bottom of the object, i.e. the draft is taken to be $0.4m$ The width of the moonpool is $0.8m$ in stream-wise (x) direction and $1.0m$ in cross-stream (y) direction. Rather than moving the moonpool through the grid or to prescribe the inflow velocity, the moonpool and the grid fixed to the geometry are accelerated from rest. The acceleration is modeled through the forcing term in the Navier–Stokes equations. No-slip boundary

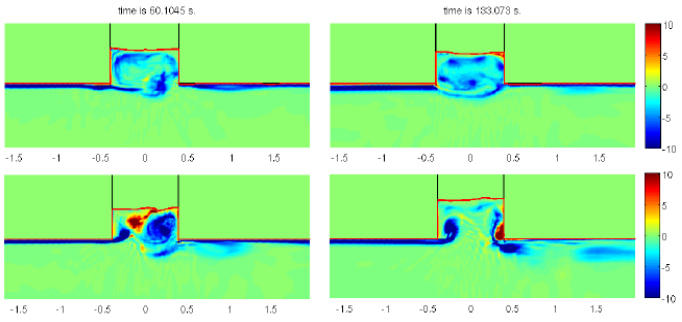

FIGURE 11. DEVELOPMENT OF VORTICITY IN TIME (FROM LEFT TO RIGHT: 60 s AND 133 s) FOR A FINAL SPEED (AFTER ACCELERATION) OF 0.7 m/s (TOP) AND 1.0 m/s (BOTTOM).

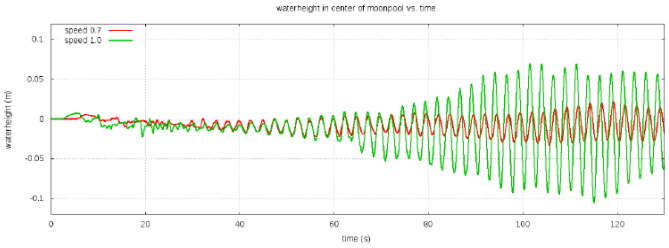

FIGURE 12. WATER HEIGHT AS A FUNCTION OF TIME FOR THE TWO FINAL SPEEDS (AFTER ACCERATION). AFTER A TIME OF ABOUT 63s, FOR THE WATER MOTION IN THE MOONPOOL AT SPEED 1.0m/s RESONANCE BEHAVIOUR IS OBSERVED.

conditions are applied at all the moonpool walls.

The moonpool is accelerated to two constant speeds: $0.7m/s$ and $1.0m/s$. The evolution of the water motion in the moonpool is illustrated by the vorticity plots in Fig. 11. In the first stage, during acceleration of the moonpool a big vortex is formed at the edge and shear layer roll-up is observed. The vortex travels upward in the moonpool and impinges on the free surface. For the lower speed $(0.7m/s)$ the vortices that are formed at the edge circulate through the moonpool, deforming the free surface and inducing a small-amplitude oscillation of the water column (the piston mode). For the higher speed $(1.0m/s)$, the elevation of the free-surface is more dramatic, which can clearly be seen from the oscillation of the water height in Fig. 12. The synchronization of vortex formation and the oscillation of the water column lead to resonant (piston mode) motion of the water in the moonpool. Moreover, a bore formed by the impinging vortex on the right-side wall of the moonpool is observed to travel back and forth between the right and left wall (slosh mode). These results are a clear improvement over a second-order upwind discretization which results in a steady state solution, with a stationary recirculation zone present in the moonpool (see the discussion in [30]). Also, traditional LES models (like the Smagorinsky model) produce a more diffusive flow pattern, with much less vortical details. It pays off that the current blended turbulence model is minimizing the amount of eddy viscosity. We hope to present a detailed comparison between the results from various turbulence models in the near future.

CONCLUSIONS

The current research developments in the free-surface flow solver ComFLOW have been demonstrated and discussed. Only a first impression of the achieved results could be presented. A more elaborate discussion will follow in three PhD-theses by the present authors, which will be published this year.

– A local grid refinement approach has been presented. Special attention was paid to designing a compact stencil, which facilitates the interface discretization near cut-cells and the modification of the Volume-of-Fluid scheme. It has been successfully applied to the simulation of wave impact problems. For a dambreak simulation, the refined (or better: coarsened) results show very good agreement with the earlier obtained fine-grid results, yet at a fraction of the calculational costs.

– Also, we studied the effect of VOF algorithms on spurious energy dissipation in propagating wave simulations. By implementing more accurate interface reconstruction/advection combinations, spurious energy dissipation as well as phase shift are reduced substantially.

– A new generating and absorbing boundary condition has been presented, based on the familiar Sommerfeld condition. The 'to-be-prescribed' phase velocity adapts itself to the actual propagation velocity of the outgoing waves.

– Improved viscous flow modelling by a blended turbulence model has been demonstrated by means of free-surface water motion in a moonpool. A symmetry-preserving second-order central discretization of the convective term was used with a minimum amount of turbulent viscosity. Even on relatively coarse grids, this turbulence model gives acceptable results which show the essential features of moonpool motion.

ACKNOWLEDGMENT

This research is supported by the Dutch Technology Foundation STW, applied science division of NWO and the technology programme of the Ministry of Economic Affairs in The Netherlands (contracts GWI.6433 and 10475).

REFERENCES

[1] Kleefsman, K.M.T., Fekken, G., Veldman, A.E.P., Iwanowski, B., and Buchner, B., 2005. "A volume-of-fluid based simulation method for wave impact problems". *Journal of Computational Physics*, **206**(1), pp. 363–393.

[2] Veldman, A.E.P., Luppes, R., Bunnik, T., Huijsmans, R.H.M., Düz, B., Iwanowski, B., Wemmenhove, R., Borsboom, M.J.A., Wellens, P.R., van der Heiden, H.J.L., and van der Plas, P., 2011. "Extreme wave impact on oshore platforms and coastal constructions". In *30th Conf. on Ocean, Offshore and Arctic Eng. OMAE2011*, Rotterdam (The Netherlands), 19-24 June 2011, paper OMAE2011-49488.

[3] G. Fekken, A.E.P. Veldman and B. Buchner, 1999. "Simulation of green-water loading using the Navier-Stokes equations". In J. Piquet (ed.) *Proceedings 7th International Conference on Numerical Ship Hydrodynamics*, Nantes (France), 19-22 July 1999, paper 12.

[4] Wemmenhove, R., Luppes, R. and Veldman, A.E.P., 2008. "Application of a VOF method to model compressible two-phase flow in sloshing tanks". *27th Conference on Offshore*

Mechanics and Arctic Engineering OMAE Conference, Estoril (Portugal), 16-19 June 2008, paper OMAE2008-57254.

[5] Verstappen, R.W.C.P., 2013. "Blended scale-separation models for large eddy simulations". In *Proceedings 14th European Turbulence Conference ETC14*, Lyon (France), September 1-4.

[6] Werner, H. and Wengle, H., 1993. "Large-eddy simulation of turbulent flow over and around a cube in a plate channel". In *8th Symposium on Turbulent Shear Flows*. SpringerVerlag, pp. 155–168.

[7] Roe, P.L., 1986. "Characteristic-based schemes for the Euler equations". *Ann. Rev. Fluid Mech.*, **18**, pp. 337–365.

[8] Higdon, R.L., 1987. "Numerical absorbing boundary conditions for the wave equation". *Mathematics of Computation*, **49**, pp. 65–90.

[9] Wellens, P.R., Luppes, R., Veldman, A.E.P. and Borsboom, M.J.A., 2009. "CFD simulations of a semi-submersible with absorbing boundary conditions". *28th Conference on Ocean, Offshore and Arctic Engineering*, Honolulu (Hawaii), 31 May - 5 June 2009, paper OMAE2009-79342.

[10] de Tullio, M.D., De Palma, P., Iaccarino, G., Pascazio, G., and Napolitano, M., 2007. "An immersed boundary method for compressible flows using local grid refinement". *Journal of Computational Physics*, **225**(2), pp. 2098–2117.

[11] Verstappen, R.W.C.P. and Veldman, A.E.P., 2003. "Symmetry-preserving discretization of turbulent flow". *Journal of Computational Physics*, **187**, pp. 343–368.

[12] Minion, M.L., 1996. "A projection method for locally refined grids". *Journal of Computational Physics*, **127**(1), pp. 158–178.

[13] Liu, Q., 2011. "A stable and accurate projection method on a locally refined staggered mesh". *International Journal for Numerical Methods in Fluids*, **67**(1), pp. 74–92.

[14] Uzgoren, E., Singh, R., Sim, J. , and Shyy, W., 2007. "Computational modeling for multiphase flows with spacecraft application". *Progress in Aerospace Sciences*, **43**(4), pp. 138–192.

[15] Losasso, F., Gibou, F., and Fedkiw, R., 2004. "Simulating water and smoke with an octree data structure". In *ACM Transactions on Graphics* (TOG), **23**, pp. 457–462.

[16] Hirt, C.W. and Nichols, B.D., 1981. "Volume of fluid (VOF) method for the dynamics of free boundaries". *Journal of Computational Physics*, **39**, pp. 201–225.

[17] Youngs, D.L., 1987. "An interface tracking method for a 3D Eulerian hydrodynamics code". AWRE Design Math. Div., AWRE/44/92/35.

[18] Rider, W.J. and Kothe, D.B., 1998. "Reconstructing volume tracking". *Journal of Computational Physics*, **141**, pp. 112–152.

[19] Pilliod, J.E. and Puckett, E.G., 2004. "Second-order accurate volume-of-fluid algorithms for tracking material interfaces". *Journal of Computational Physics*, **199**, pp. 465–502.

[20] Leonard, B.P., Lock, A.P. and MacVean, M.K., 1996. "Conservative explicit unrestricted time-step multidimensional constancy-preserving advection schemes". *Monthly Weather Review*, **124**, pp. 2588–2606.

[21] Gerrits, J., 2001. "Dynamics of liquid-filled spacecraft". Ph.D. Thesis, University of Groningen, The Netherlands.

[22] Aulisa, E., Manservisi, S., Scardovelli, R. and Zaleski, S., 2007. "Interface reconstruction with least-squares fit and split advection in three-dimensional Cartesian geometry". *Journal of Computational Physics*, **225**, pp. 2301–2319.

[23] Scardovelli, R. and Zaleski, S., 2000. "Analytical relations connecting linear interfaces and volume fractions in rectangular grids". *Journal of Computational Physics*, **164**, pp. 228–237.

[24] Givoli, D., 1991. "Non-reflecting boundary conditions". *Journal of Computational Physics*, **94**, pp. 1–29.

[25] Verstappen, R.W.C.P., 2011. "When does eddy viscosity damp subfilter scales sufficiently?" *Journal of Scientific Computing*, **49**(1), pp. 94–110.

[26] Sagaut, P., 2001. "*Large Eddy Simulation for Incompressible Flows*". Springer-Verlag.

[27] Verstappen, R.W.C.P., 2008. "On restraining the production of small scales of motion in a turbulent channel flow". *Computers and Fluids*, **37**(7), pp. 887–897.

[28] Trias, F.X. and Verstappen, R.W.C.P., 2011. "On the construction of discrete filters for symmetry-preserving regularization models". *Computers and Fluids*, **40**(1), pp. 139–148.

[29] Trias, F.X., Verstappen, R.W.C.P., Gorobets, A., Soria, M. and Oliva, A., 2010. "Parameter-free symmetry-preserving regularization modeling of a turbulent differentially heated cavity". *Computers and Fluids*, **39**(10), pp. 1815–1831.

[30] Gaillarde, G. and Cotteleer, A., 2005. "Water motion in moonpools: empirical and theoretical approach". Technical report, Maritime Research Institute Netherlands (MARIN), HMC Heerema.